

# New bright soft X-ray selected ROSAT AGN

## II. Optical emission line properties\*

D. Grupe<sup>1,2,\*\*</sup>, K. Beuermann<sup>1,2</sup>, K. Mannheim<sup>2</sup>, and H.-C. Thomas<sup>3</sup>

<sup>1</sup> MPI für Extraterrestrische Physik, Giessenbachstrasse, 85748 Garching, Germany

<sup>2</sup> Universitäts-Sternwarte, Geismarlandstrasse 11, 37083 Göttingen, Germany

<sup>3</sup> MPI für Astrophysik, Karl-Schwarzschild-Strasse 1, 85748 Garching, Germany

Received 18 May 1998 / Accepted 3 August 1999

**Abstract.** We present the emission line properties of a sample of 76 bright soft X-ray selected ROSAT Active Galactic Nuclei. All optical counterparts are Seyfert 1 galaxies with rather narrow permitted lines, strong optical FeII line blends, and weak forbidden lines. By selection, they also have steep soft X-ray spectra when compared with typical Seyfert 1 galaxies. We discuss possible origins of these peculiar trends employing detailed correlation analyses, including a Principal Component Analysis. The optical spectra are presented in the Appendix.

**Key words:** accretion, accretion disks – galaxies: active – galaxies: nuclei – galaxies: Seyfert – galaxies: quasars: general

### 1. Introduction

The optical/UV/soft X-ray bump has turned out to be a common property of most Seyfert 1 type Active Galactic Nuclei (AGN). With ROSAT (Trümper 1983) numerous AGN have been found that show a soft X-ray excess, commonly believed to be the high energy part of the “Big Blue UV/Soft X-ray Bump”.

Before ROSAT, a study of soft X-ray selected AGN had to rely on serendipitous observations, notably with the EINSTEIN Image Proportional Counter (IPC). In a sample of 53 AGN from the Ultra Soft Survey (USS) of Córdova et al. (1992), Puchnarewicz et al. (1992) found preferentially AGN with relatively narrow permitted emission lines and strong FeII emission. About half of their sample had  $\text{FWHM}(\text{H}\beta) < 2000 \text{ km s}^{-1}$ , confirming the earlier finding that X-ray selected AGN tend to show relatively narrow permitted lines (Stephens 1989). Such AGN were defined by Osterbrock & Pogge (1985) as “narrow-line” Seyfert 1 galaxies (NLSy1). Boller et al. (1996) found

vice versa that optically selected NLSy1 galaxies show very steep X-ray spectra, confirming the physical relation between these properties (see also Boroson & Green 1992, Brotherton 1996, Laor et al. 1994, 1997, Brandt & Boller 1998).

The present sample of 76 AGN results from the optical identification of the brightest previously unknown soft X-ray sources at high galactic latitude (Thomas et al. 1998, Beuermann et al. 1999) found in the ROSAT All-Sky Survey, RASS (Voges 1993, Voges et al. 1999). By definition, it excludes well-known sources<sup>1</sup>.

In Paper I (Grupe et al. 1998a) we described the continuum properties of the 76 AGN contained in the sample. The mean soft X-ray spectral slope is steeper ( $\langle \alpha_X \rangle = 2.1$ ,  $F_\nu \propto \nu^{-\alpha}$ ) than found in other AGN studies. At optical wavelengths, the soft AGN have significantly bluer spectra than a comparison sample comprised of AGN with a canonical, much harder X-ray spectrum, whereas the slope between 5500 Å and 1 keV is the same. This implies stronger Big Blue Bump emission relative to an underlying continuum. The blueness of the optical spectra increases with the softness of the X-ray spectra *and* with the luminosity, saturating at an approximate  $F_\nu \propto \nu^{+0.3}$  spectrum and consistent with most of the Big Blue Bump emission originating in an (comptonized) accretion disk and stretching from optical wavelengths to the soft X-ray regime.

In this paper we investigate the properties of the optical emission lines of the bright soft X-ray selected AGN and discuss their connection with X-ray properties. Results are compared with a control sample of hard X-ray selected ROSAT AGN (see Grupe 1996 and Paper I) with optical data taken from the literature and ROSAT Position Sensitive Proportional Counter (PSPC, Pfeiffermann et al. 1986) pointed observations retrieved from the ROSAT public archive at the ROSAT Sci-

Send offprint requests to: D. Grupe (dgrupe@xray.mpe.mpg.de)

\* Based in part on observations at the European Southern Observatory La Silla (Chile) with the 2.2m telescope of the Max-Planck-Society during MPG and ESO time. All spectra can be retrieved via CDS anonymous FTP 130.79.128.5.

\*\* Guest Observer, McDonald Observatory, University of Texas at Austin

<sup>1</sup> The initial selection criteria of the sample were a total PSPC count rate  $> 0.5 \text{ cts/s}$ , a negative hardness ratio HR1 of the spectral energy distribution, a source location at galactic latitudes  $|b| > 20^\circ$ , and sufficient previous knowledge of the optical counterpart (see the identification papers by Thomas et al. 1998 and Beuermann et al. 1999). Based on the final (and different) count rates given the RASS Bright Source Catalog (Voges et al. 1999), the sample is no longer complete in a flux-limited sense.

ence Data Center at MPE Garching. Sect. 2 deals with the observations and data reduction. Several diagnostically important correlations between emission-line and continuum properties are noted in Sect. 3. Finally, we discuss the results in Sect. 4 addressing the issue of the origin of the difference between Seyfert 1 and NLSy1 galaxies. In the Appendix we present the optical medium-resolution spectra of the AGN as well as the FeII subtracted spectra.

Throughout the paper, luminosities are calculated assuming a Hubble constant of  $H_0 = 75 \text{ km s}^{-1} \text{ Mpc}^{-1}$  and a deceleration parameter of  $q_0 = 0$ .

## 2. Observations and data reduction

### 2.1. Observations

The statistical analysis of the RASS X-ray data was presented in Paper I. There, we also discussed the overall spectral energy distribution based on the X-ray data and the optical continuum inferred from the spectrophotometry presented here. The optical continuum slope is defined between rest-frame wavelengths of 4400 and 7000 Å.

We have performed medium resolution ( $\sim 5 \text{ Å FWHM}$ ) optical spectroscopy for all AGN of the sample, using the 2.2m MPI/ESO telescope at La Silla, Chile and the 2.1m telescope at McDonald Observatory of the University of Texas at Austin. The flux-calibrated spectra of all 76 ROSAT AGN summarized in Appendix A: and spectral parameters listed in Table A1. The positions quoted for the optical counterparts were derived from the Digitized Sky Survey. Table A1 also provides information on the instrumentation used, the exposure times, etc. The spectra are published electronically at the anonymous FTP 130.79.128.5.

### 2.2. FeII subtraction

All Seyfert 1 galaxies in the soft X-ray AGN sample show optical FeII emission. The optical FeII emission is dominated by two blends, between 4435–4700 Å in the blue, and between 5070–5600 Å in the red. Weaker highly ionized iron lines like [FeVII]λ5159 or λ5721 or even the HeIIλ4686 line are blended with this emission. These blends also contaminate strong lines such as [OIII]λλ4959,5007. In order to reliably measure line fluxes and to determine the strength of the FeII emission it is necessary to appropriately model the FeII complexes. We adopt the method described by Boroson & Green (1992) and used the FeII template of I Zw 1 given in their paper for the wavelength range  $\sim 4400\text{--}6000 \text{ Å}$ . In order to correct also for the bluer part of the spectrum, this template was extended towards shorter wavelengths by using the relative FeII line intensities given by Phillips (1978a,b). The whole template was wavelength-shifted according to the redshift of the object spectrum and the individual FeII lines were broadened to the FWHM of the broad Hβ line by using a Gaussian filter. The template was scaled to match the line intensities of the object spectrum and then subtracted. It was found most reliable to scale the template by fitting the intensities of the FeII lines at 4924 and 5018 Å.

In order to determine the rest-frame equivalent width of FeII, we measured the flux in the scaled template between the rest wavelength 4250 Å and 5880 Å, and the continuum flux density at 5050 Å in the FeII subtracted spectra. All spectra can be accessed by anonymous FTP 130.79.128.5.

### 2.3. Other line measurements

The FeII-subtracted spectra were used to measure the non-FeII line properties. In these spectra, Hβ is still a mixture of broad and narrow components which we attempt to separate for further analysis. In the spectra of some objects of subtype Sy1.5 this is straightforward, in others both components are not easily separable. In order to isolate the broad Hβ component as best as possible in all spectra, we proceed as follows. We use a template built from the [OIII]λ5007 line which includes the asymmetry often found in this and other narrow lines. The Hβ line was then synthesized from this narrow and a broader Gaussian component. The latter is referred to as Hβ<sub>b</sub>. The FWHM(Hβ<sub>b</sub>) is what we consider as representative of the Broad Line Region (BLR). We chose to define the [OIII]λ5007/Hβ<sub>b</sub> ratio such that it refers to the broad component Hβ<sub>b</sub>. Finally, the instrumental resolution was determined from the FWHM of the night-sky lines and all quoted line widths were corrected for the instrumental resolution.

Deriving the Balmer decrement Hα/Hβ requires correction of Hα for the contributions of both, the narrow Hα component and the [NII]λλ6548,6584 lines. In many cases, however, it proved difficult to isolate the broad Hα component this way. In order to correct for the contributions of [NII]λλ6548,6584 we assumed, therefore, that these lines contribute 35% of the flux in [OIII]λ5007, following Ferland & Osterbrock (1986). We refrained from separating broad and narrow Balmer components and measured the Balmer decrement from the total (broad and narrow) fluxes in Hα and Hβ. These values of the Balmer decrements do not differ appreciably from those of the broad components because the relative contributions of the narrow components to the Balmer line fluxes is usually small. Our Balmer decrements are not necessarily representative of the narrow components.

### 2.4. Continuum measurements

Most of the V-magnitudes in Table 1 were derived from our spectrophotometry. Although the spectral fluxes were corrected as carefully as possible for slit losses in flux, the absolute fluxes are uncertain by some 0.2 mag. For 22 southern objects, we determined more accurate V-magnitudes from CCD photometry (see Thomas et al. 1998). In this paper, we do not distinguish between the different sources of V, because the intrinsic scatter in the data is larger than that produced by errors in measuring the optical fluxes. The optical continuum slope  $\alpha_{\text{opt}}$  is measured between 4400–7000 Å in the rest frame. The X-ray spectral slope  $\alpha_x$  is defined between 0.2 and 2.0 keV (see Paper I for more details).

**Table 1.** Optical results of the AGN. The FWHM are given in  $\text{km s}^{-1}$ , equivalent width EW of FeII in  $\text{\AA}$  in the rest-frame, and the luminosity of  $H\beta_b$  in Watt

No.	Object	V	z	FWHM		EW FeII	$\frac{H\alpha}{H\beta}$	$\log$ $\frac{[OIII]}{H\beta}$	$\log$ $\frac{FeII}{H\beta}$	$\log$ $\frac{FeII}{[OIII]}$	$\log$ $L_{H\beta}$	Notes
				$H\beta$	[OIII]							
1	RX J0022-34	16.1	0.219	4110± 120	355± 10	60	3.5	-0.40	-0.17	+0.23	36.1	
2	ESO 242-G8	16.1	0.059	3670± 160	310± 10	140	5.9	-0.09	+0.28	+0.37	34.7	
3	WPVS 007	14.8	0.029	1620± 50	320± 40	215	3.6	-0.82	+0.68	+1.50	34.5	
4	RX J0057-22	14.5	0.062	1380± 100	630± 160	185	3.3	-0.90	+0.72	+1.62	35.1	
5	QSO 0056-36	15.1	0.165	4700± 160	435± 80	120	3.6	-1.21	+0.28	+1.49	36.0	
6	RX J0100-51	15.4	0.062	3450± 120	565± 30	200	2.7	-0.49	+0.55	+1.04	34.9	
7	MS 0117-28	16.0	0.349	2925± 100	895± 200	170	2.5	-1.25	+0.59	+1.84	36.3	
8	IRAS 01267-21	15.4	0.093	2900± 100	410± 20	205	3.0	-0.53	+0.44	+0.97	35.4	
9	RX J0134-42	16.0	0.237	1160± 80	—	175	4.0	-1.32	+1.09	+2.42	35.3	1
10	RX J0136-35	18.0	0.289	1320± 120	870± 340	285	4.2	-0.64	+0.92	+1.57	35.1	
11	RX J0148-27	15.5	0.121	1250± 100	765± 360	315	3.4	-1.09	+0.69	+1.77	35.5	
12	RX J0152-23	15.6	0.113	3510± 130	680± 30	215	2.8	-0.30	+0.50	+0.80	35.5	
13	RX J0204-51	16.6	0.151	5990± 240	310± 20	170	4.3	-0.52	+0.22	+0.75	35.5	
14	RX J0228-40	15.2	0.494	2265± 100	700± 120	215	4.0	-1.30	+0.64	+1.94	37.0	
15	RX J0319-26	15.9	0.079	4170± 240	480± 40	235	3.9	-0.51	+0.60	+1.11	35.0	
16	RX J0323-49	16.5	0.071	2075± 70	230± 20	205	4.4	-0.66	+0.52	+1.18	34.7	
17	ESO 301-G13	15.5	0.064	3180± 200	545± 20	195	2.9	+0.15	+0.36	+0.21	35.1	
18	VCV 0331-37	16.3	0.064	2165± 60	170± 10	205	3.2	-0.59	+0.39	+0.98	34.8	
19	RX J0349-47	16.8	0.299	2250± 150	635± 60	530	3.5	-0.50	+0.64	+1.14	36.0	
20	Fairall 1116	15.2	0.059	4560± 120	320± 20	130	3.5	-0.67	+0.20	+0.88	35.2	
21	RX J0412-47	15.9	0.132	5580± 400	70± 10	45	5.8	-0.17	-0.09	+0.08	35.5	2
22	RX J0426-57	14.1	0.104	2900± 100	450± 10	30	4.2	+0.13	-0.39	-0.52	36.0	2
23	Fairall 303	16.2	0.040	1720± 60	140± 10	370	—	-0.57	+0.48	+1.04	34.5	
24	RX J0435-46	17.1	0.070	3820± 240	260± 20	190	3.7	-0.16	+0.77	+0.93	34.2	
25	RX J0435-36	17.1	0.141	6750± 620	810± 40	240	3.5	-0.06	+0.57	+0.63	35.0	
26	RX J0437-47	15.3	0.052	4215± 120	240± 20	130	3.2	-0.71	+0.38	+1.08	34.9	
27	RX J0438-61	15.7	0.069	2410± 100	190± 10	155	3.8	-0.22	+0.19	+0.42	35.2	
28	RX J0439-45	16.6	0.224	2105± 100	1020± 240	210	3.5	-0.77	+0.65	+1.42	35.6	
29	RX J0454-48	17.7	0.363	1970± 200	—	265	4.4	—	+0.74	—	35.6	3
30	RX J1005+43	16.4	0.178	2990± 120	825± 150	330	—	-0.95	+0.89	+1.85	35.4	
31	CBS 126	15.4	0.079	2850± 200	370± 20	110	3.5	-0.59	+0.13	+0.72	35.3	
32	RX J1014+46	17.1	0.324	—	—	230	—	—	—	—	—	4
33	RX J1017+29	15.7	0.049	1990± 200	255± 20	105	—	-0.16	+0.65	+0.81	34.3	
34	Mkn 141	15.1	0.042	4175± 340	395± 30	125	3.8	-0.34	+0.61	+0.95	34.5	
35	Mkn 142	15.2	0.045	1790± 70	280± 30	285	3.3	-0.72	+0.77	+1.49	34.7	
36	RX J1050+55	16.7	0.333	—	—	355	—	—	—	—	—	4
37	EXO 1055+60	16.9	0.149	2155± 100	540± 50	365	—	-0.53	+0.68	1.22	35.2	
38	RX J1117+65	16.4	0.147	2160± 110	880± 150	260	—	-0.67	+0.77	+1.44	35.2	
39	Ton 1388	14.4	0.177	2920± 80	920± 150	190	4.6	-1.04	+0.50	+1.54	36.3	
40	Mkn 734	14.4	0.033	2230± 140	450± 10	235	3.2	-0.31	+0.66	+0.97	34.8	
41	Z 1136+34	16.0	0.033	1685± 80	210± 20	260	—	-0.57	+0.56	+1.13	34.3	
42	CSO 109	16.3	0.059	2270± 240	230± 20	185	—	-0.30	+0.95	+1.25	34.2	
43	RX J1231+70	16.0	0.208	3990± 150	550± 60	50	—	-0.41	+0.11	+0.52	35.7	2, 5
44	IC 3599	16.5	0.021	635± 100	580± 30	65	4.2	+0.50	+0.91	+0.40	32.8	2
45	IRAS 1239+33	15.1	0.044	1900± 150	485± 30	200	5.9	+0.33	+0.85	+0.52	34.4	
46	RX J1312+26	16.2	0.061	2905± 220	205± 30	115	—	-0.82	+0.60	+1.42	34.4	
47	RX J1314+34	16.3	0.075	1590± 100	400± 50	250	—	-0.58	+0.71	+1.29	34.7	
48	RX J1355+56	16.5	0.122	1780± 170	580± 20	160	—	+0.21	+0.52	+0.30	35.0	
49	RX J1413+70	16.9	0.107	5170± 400	395± 30	150	—	+0.08	+0.60	+0.52	34.7	
50	Mkn 684	14.7	0.046	1685± 100	405± 80	240	3.1	-0.80	+0.92	+1.72	34.7	
51	Mkn 478	14.6	0.077	1915± 90	610± 110	290	3.7	-0.78	+0.72	+1.50	35.5	
52	RX J1618+36	16.6	0.034	830± 80	100± 10	100	—	-0.22	+0.77	+0.99	33.5	
53	RX J1646+39	17.1	0.100	2160± 130	230± 20	255	—	-0.50	+0.62	+1.12	34.7	
54	RX J2144-39	18.0	0.140	1445± 120	210± 20	130	4.2	-0.07	+0.71	+0.78	34.4	
55	RX J2154-44	15.8	0.344	2655± 100	510± 50	100	4.1	-0.78	+0.23	+1.01	36.4	

Table 1. (continued)

No.	Object	V	z	FWHM		EW FeII	$\frac{H\alpha}{H\beta}$	$\log \frac{[OIII]}{H\beta}$	$\log \frac{FeII}{H\beta}$	$\log \frac{FeII}{[OIII]}$	$\log L_{H\beta}$	notes
				H $\beta$	[OIII]							
56	RX J2213–17	17.2	0.146	1625±200	250± 70	160	5.4	+0.30	+0.74	+0.44	34.8	
57	RX J2216–44	15.8	0.136	2200± 80	695± 70	250	3.1	–0.69	+0.69	+1.38	35.5	
58	RX J2217–59	16.2	0.160	1850±100	1075±150	330	3.4	–0.51	+0.99	+1.49	35.2	
59	RX J2221–27	17.7	0.177	2090±100	465± 40	265	3.5	–0.52	+0.53	+1.04	35.3	
60	RX J2232–41	16.9	0.075	4490±350	455± 20	130	3.6	–0.19	+0.20	+0.39	34.7	
61	RX J2241–44	15.8	0.545	1890±200	380±100	210	—	–0.94	+0.90	+1.84	36.5	
62	RX J2242–38	16.9	0.221	2210± 70	560± 60	430	2.7	–0.76	+0.62	+1.38	35.7	
63	RX J2245–46	14.8	0.201	2760±140	680± 60	205	3.4	–0.46	+0.52	+0.97	36.4	
64	RX J2248–51	15.5	0.102	3460±200	230± 10	100	4.4	+0.02	+0.23	+0.21	35.5	
65	MS 2254–37	15.0	0.039	1545± 70	610± 50	90	4.4	–0.44	+0.28	+0.72	34.7	
66	RX J2258–26	16.1	0.076	2815±180	285± 10	185	3.8	+0.15	+0.36	+0.22	35.0	
67	RX J2301–55	15.4	0.140	2590±120	355± 80	230	3.7	–1.08	+0.71	+1.78	35.6	
68	RX J2303–55	17.5	0.084	4030±200	495± 60	160	3.9	–0.75	+0.71	+1.46	34.2	
69	RX J2304–35	16.6	0.042	1775±130	210± 10	110	5.4	+0.39	+0.66	+0.27	34.0	
70	RX J2304–51	17.2	0.106	3830±160	190± 10	85	3.1	–0.05	–0.16	–0.11	35.0	
71	RX J2317–44	16.8	0.134	1390± 35	350± 50	310	3.9	–0.76	+0.58	+1.34	35.2	
72	RX J2325–32	17.0	0.216	3295±130	220± 10	145	4.6	–0.43	+0.01	+0.44	35.8	
73	RX J2340–53	17.6	0.321	1880±120	710± 90	285	2.8	–0.57	+0.59	+1.15	35.7	
74	MS 2340–15	15.6	0.137	1565± 80	760± 70	175	3.5	–0.86	+0.61	+1.47	35.5	
75	RX J2349–33	16.6	0.144	7715±850	560± 10	355	4.2	+0.42	+0.11	–0.30	35.9	2
76	RX J2349–31	16.6	0.135	5210±270	475± 20	95	3.0	–0.15	+0.40	+0.54	35.1	

Table notes:

1. In an optical spectrum of 5 hours exposure (Grupe et al., in preparation), weak [OIII] $\lambda$ 5007 is visible.
2. Quantities referring to FeII are upper limits.
3. [OIII] is not in the observed wavelength range.
4. H $\beta$  and [OIII] are not in the observed wavelength range.
5. [OIII] measurements are based on the [OIII] $\lambda$ 4959 line.

### 3. Results

All objects in our sample were found to be Seyfert 1 type AGN. We do not divide the Seyfert 1 class into subclasses such as NLSy1s or Seyfert 1.5<sup>2</sup>. This soft X-ray selected sample includes only one possible Sy 2 object, the X-ray transient IC 3599 which was discussed by Brandt et al. (1995) and Grupe et al. (1995a, 1998b). Recently, this object has been classified as a Seyfert 1.9 by Komossa & Bade (1999).

The distribution of the H $\beta$  line width of the objects in our sample of soft X-ray selected AGN shows a preference for rather

<sup>2</sup> The definitions underlying Seyfert classifications depend on the resolution of and the noise in the spectra used. For instance, with increasing resolution, NLR emission components will be found in Seyferts which defied such detection with lower resolution, causing the definition of a certain object as Seyfert 1.5 or NLSy1 to become fuzzy (see also Goodrich 1989a,b). A dividing line at 2000 km s<sup>–1</sup> is generally used to separate Sy1 and NLSy1, although many objects display NLSy1 properties in spite of their FWHM(H $\beta_b$ ) somewhat exceeding this value (e.g. Ton 1388). Furthermore, published values of FWHM(H $\beta_b$ ) do not always refer to the same component (ideally the broad one) of H $\beta$ . For these reasons, we relax our language in the following referring to Narrow-Line Seyfert 1 galaxies as Sy1 galaxies with narrow BLR emission lines, weak [OIII]/H $\beta_b$  ratio, strong FeII emission, and steep X-ray spectra when compared with canonical Sy1s.

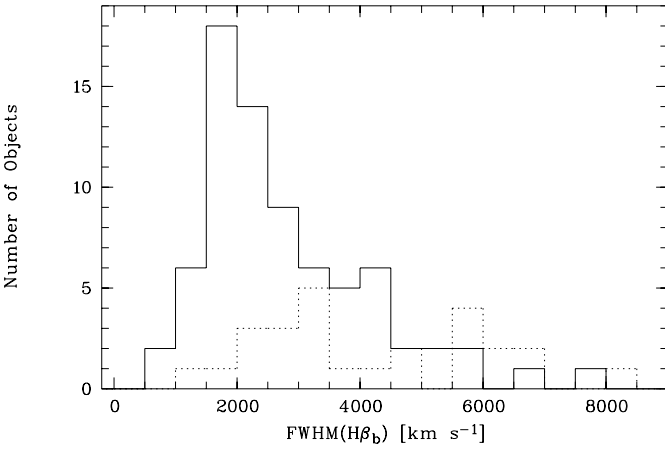
narrow permitted emission lines. The average line width is significantly smaller than that of the objects from the comparison sample of hard X-ray selected Seyfert galaxies. The distributions of the FWHM of the broad components of H $\beta$  in both samples are displayed in Fig. 1. We find mean values of 2790±160 (median 2250) km s<sup>–1</sup> and 4210±360 (median 3460) km s<sup>–1</sup>, for the soft and hard sample, respectively. Because some of the spectra of the hard X-ray objects given in the literature are rather poor we may have underestimated the widths of the broad components and the real difference may be even larger. We again emphasize that our FWHM refer to the broad component in H $\beta$  only, while many values quoted in the literature refer to the whole line and may underestimate the FWHM of the underlying broad component.

#### 3.1. Correlations

In this section we show the results of correlation analyses performed on parameters measured from the individual emission lines. The methods used include the Principal Component Analysis (PCA, see Sect. 3.2 below) which is helpful in identifying the nature of the physical parameters responsible for the observed correlations between observed parameters. We also present results of a Spearman rank order test in Table 2. Correla-

**Table 2.** Results of the the non-parametric Spearman rank order test. The lower left of the table lists the correlation coefficients and the upper right the significance levels obtained from Student’s t test, respectively.

Prop	FWHM( $H\beta_b$ )	FWHM([OIII])	$\frac{[\text{OIII}]}{H\beta_b}$	EW FeII	$\alpha_x$	$\alpha_{\text{opt}}$	$\alpha_{\text{ox-soft}}$	$\nu L_V$	$\nu L_{250\text{eV}}$	$\frac{H\alpha}{H\beta}$
FWHM( $H\beta_b$ )	—	-0.5	+2.0	-2.8	-3.3	+0.3	+1.5	+1.1	+0.3	-0.6
FWHM([OIII])	-0.06	—	-2.5	+3.2	+2.4	-1.9	-0.6	+5.4	+4.8	-2.3
[OIII]/ $H\beta_b$	+0.23	-0.29	—	-3.3	-2.6	+6.0	-1.1	-3.8	-3.2	+2.2
EW FeII	-0.31	+0.36	-0.36	—	+1.9	-1.1	-0.9	+1.3	+1.6	-2.2
$\alpha_x$	-0.36	+0.27	-0.29	+0.22	—	-4.1	-4.1	+3.1	+5.8	+0.3
$\alpha_{\text{opt}}$	+0.04	-0.22	+0.58	-0.13	-0.43	—	+0.4	-5.5	-5.5	+1.6
$\alpha_{\text{ox-soft}}$	+0.17	-0.07	-0.13	-0.10	-0.44	+0.05	—	+0.2	-4.0	-0.7
$\nu L_V$	+0.13	+0.54	-0.41	+0.15	+0.34	-0.54	+0.02	—	+15.2	-0.8
$\nu L_{250\text{eV}}$	+0.04	+0.50	-0.35	+0.18	+0.56	-0.54	-0.42	+0.87	—	-0.0
$\frac{H\alpha}{H\beta}$	-0.08	-0.29	+0.27	-0.27	+0.04	+0.21	-0.09	-0.10	-0.00	—
# of objects	74	72	73	76	76	76	76	76	76	61

**Fig. 1.** Distribution of the FWHM of  $H\beta_b$  for the soft X-ray selected AGN (solid line) and the hard the X-ray comparison sample (dotted line)

tions among the continuum properties were already discussed in Paper I and are quoted here only for comparison where needed.

### 3.1.1. FWHM( $H\beta_b$ ) – $\alpha_x$ correlation

An anti-correlation in the line width of  $H\beta_b$  and the X-ray slope  $\alpha_x$  is known from studies of optically selected NLSy1 galaxies (e.g., Boller et al. 1996) and quasars (Laor et al. 1997) and is prominent also in our sample of soft X-ray selected AGN (Fig. 2). We find that only objects with comparatively narrow  $H\beta_b$  emission lines have steep X-ray spectra. Objects with broad  $H\beta_b$  lines always have harder X-ray spectra. A similar result was found by Boller et al. (1996). A Spearman rank order test yields a correlation coefficient of  $r_s = -0.36$ , corresponding to a significance level of Student’s t-test of  $t = -3.3$  or a probability of 0.001 of finding this result in random data (see Table 2). Dividing our sample into two subsamples with the dividing line at the average X-ray luminosity,  $\log \nu L_V = 37.15$  (in Watts,

see Paper I), we find that the correlation is more pronounced among the AGN with higher luminosity where the significance becomes  $r_s = 0.59$  ( $t = -4.1$ ) for the soft X-ray selected AGN alone and  $r_s = -0.71$  ( $t = -6.4$ ) for the hard and soft X-ray selected AGN together. The latter result is reminiscent of that found by Laor et al. (1997). The correlation is much weaker or absent among the low-luminosity objects. Whatever causes the differences in  $\alpha_x$  in the ROSAT bandpass, it must be a property of the AGN itself rather than of the host galaxies, since FWHM( $H\beta_b$ ) and  $\alpha_x$  both refer to nuclear properties. The object with the steepest X-ray spectrum, WPVS007 (FWHM( $H\beta_b$ )=1620 km s<sup>-1</sup> and  $\alpha_x = 8.0$ , Grupe et al. 1995b) is off scale in Fig. 2, but is included in the correlation analysis.

### 3.1.2. FWHM([OIII]) – luminosity correlation

The correlations between the FWHM([OIII]) and the optical luminosity as well as the X-ray luminosity at 250 eV are significant at the  $t \sim 5$  level. Fig. 3 displays the correlation between the [OIII] line width and the optical luminosity.

### 3.1.3. Correlations involving [OIII]/ $H\beta_b$

We find an anti-correlation between the flux ratio [OIII]/ $H\beta_b$  and the equivalent width of FeII with a correlation coefficient  $r_s = -0.36$  ( $t = -3.3$ ). Such correlation is already known from other studies (e.g. Boroson & Green 1992, or Laor et al. 1997). There is also a strong correlation between [OIII]/ $H\beta_b$  and the optical continuum slope  $\alpha_{\text{opt}}$  with  $r_s = 0.58$  ( $t = 6.0$ ). Fig. 4 shows both results.

### 3.1.4. Internal absorption

In order to check which effect internal absorption in the AGN may have on some of our results, we searched for correlations (i) between the optical continuum slope and the Balmer decrement  $H\alpha/H\beta$  and (ii) between the column density of cold absorbing

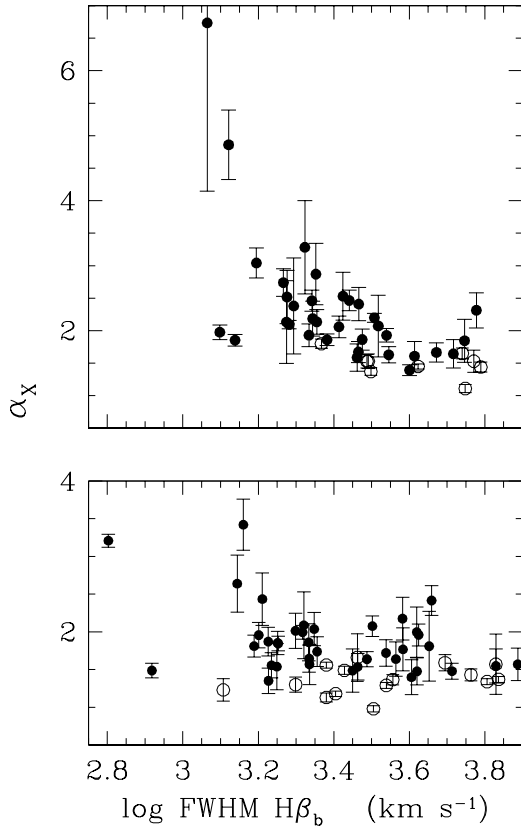


**Fig. 2.** X-ray slope  $\alpha_x$  vs.  $\text{FWHM}(\text{H}\beta_b)$ . The upper graph shows the high-luminosity AGN with  $\log \nu L_V > 37.15$  Watt. The soft X-ray AGN are displayed as solid and the hard X-ray AGN open circles. The lower graph shows the low-luminosity soft X-ray AGN with  $\log \nu L_V < 37.15$ . The AGN with the steepest X-ray spectrum, WPVS007, is off the plot ( $\text{FWHM}(\text{H}\beta_b)=1620 \text{ km s}^{-1}$ ,  $\alpha_x=8.0$ )

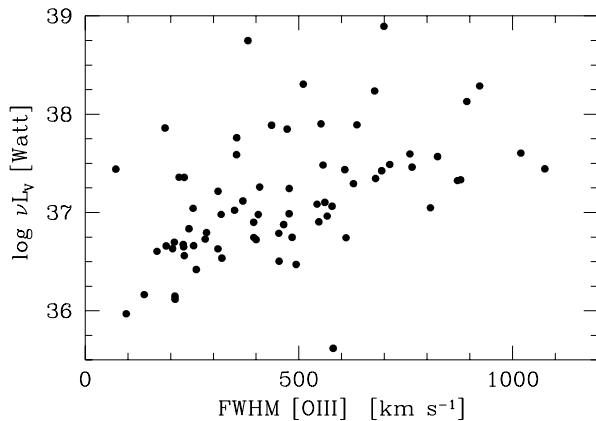


**Fig. 3.**  $\text{FWHM}[\text{OIII}]$  vs. optical monochromatic luminosity  $\log \nu L_V$

matter as derived from the X-ray spectra and the Balmer decrement. None was found, suggesting that internal absorption does not seriously affect our results. This is demonstrated in Fig. 5 and Table 2 where the quantity  $\Delta N_H$  represents the difference between the hydrogen column density determined from an absorbed power-law fit to the X-ray spectrum and the total galactic column density of atomic hydrogen (see Paper I). The mean of

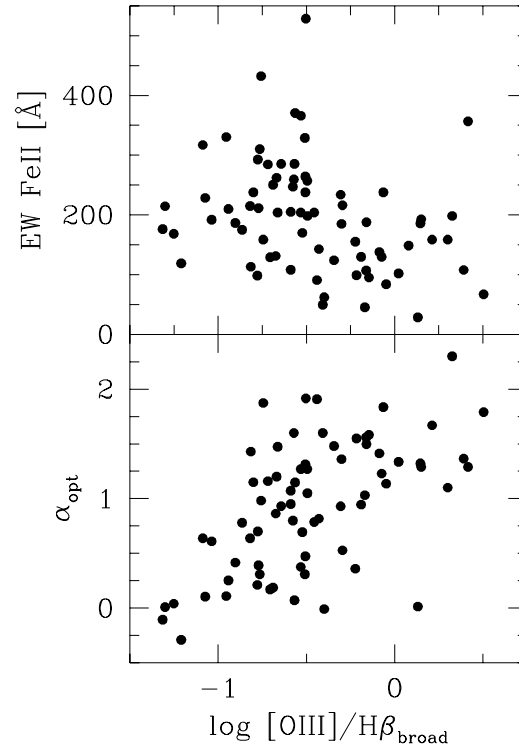


**Fig. 4.**  $[\text{OIII}]/\text{H}\beta_{\text{broad}}$  vs.  $\text{EW FeII}$  and  $\alpha_{\text{opt}}$ . A small value of  $\alpha_{\text{opt}}$  means a blue continuum and a high value represents a steeper, redder optical spectrum

the measured Balmer decrements is  $\text{H}\alpha/\text{H}\beta = 3.80 \pm 0.10$  (median 3.66) which is not far from the case B value 3.10 (e.g. Osterbrock 1989). Although case B may not be applicable in our case, the majority of the soft X-ray selected AGN is not substantially reddened. This is also consistent with the finding that only the object with the highest Balmer decrement, IRAS F12397+3333, is polarized, while all other members of the sample show are marginally polarized or not at all (Grupe et al. 1998b).

### 3.2. Principal component analysis

The appearance of AGN is governed by several underlying physical parameters. Correlation analyses between two observational quantities can reveal only part of the picture. Principal Component Analysis (PCA) is a method by which information on the underlying physical parameters can be obtained. It is based on a transformation to the principal axes of the ellipsoid formed by the data points in  $n$ -dimensional space. PCA reduces the number of relevant components and these remaining components are considered more basic than the observed properties and more astrophysically meaningful such as, in fortunate circumstances, the mass of the central black hole or the accretion rate. PCA was originally used in social studies but has been successfully applied in astrophysics as well (see e.g. Whitney 1983a,b, Boroson & Green 1992, Francis et al. 1992, Brotherton 1996).

The PCA was applied to 72 objects using the following quantities: the  $\text{FWHM}$  of  $\text{H}\beta_b$  and  $[\text{OIII}]$ , the flux ratio  $[\text{OIII}]/\text{H}\beta_b$ ,

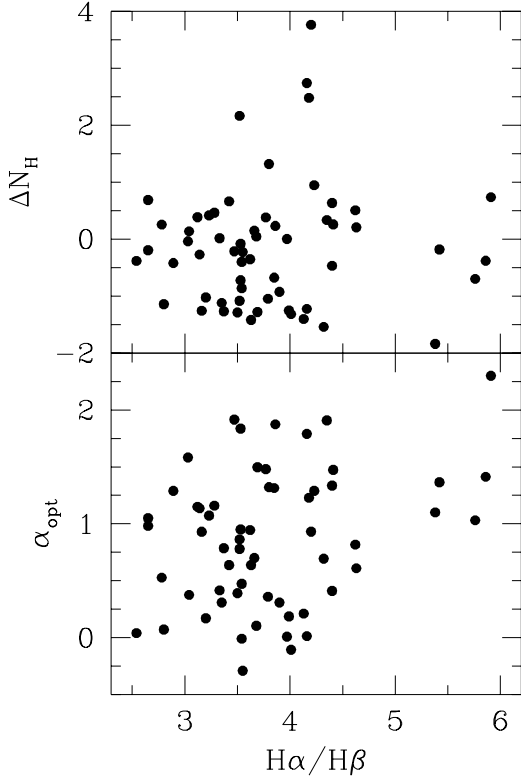


**Fig. 5.** Balmer decrement  $H\alpha/H\beta$  vs.  $\Delta N_H$  and  $\alpha_{opt}$

the equivalent width of FeII, the X-ray spectral index  $\alpha_x$ , the spectral index  $\alpha_{opt}$  of the optical continuum, and  $\log \nu L_V$ . The results are presented in Table 3. We find that the first principal component accounts for 40% of the intrinsic variance of the input parameters and, hence, seems to be an important underlying parameter that governs the observed properties of the AGN. Also the second and third components are still strong. The first three components together account for more than 70% of the variance. The first component has a strong effect on  $FWHM([OIII])$ ,  $[OIII]/H\beta_b$ ,  $\alpha_{opt}$ , and the luminosity (see Table 3). It does not, however, show the correlation between  $\alpha_x$  and  $FWHM(H\beta_b)$ . This result differs from that of Boroson & Green (1992) and Laor et al. (1997) who found that this correlation affects their Eigenvector 1. We have shown that the  $\alpha_x$ - $FWHM(H\beta_b)$  correlation is present for the high-luminosity AGN but does not appear in the low-luminosity fraction of our sample (see Fig. 2) and, by introducing subsamples with different cuts in luminosity, we confirmed that this is indeed the reason for the difference to the Boroson & Green and Laor et al. results.

#### 4. Discussion

Soft X-ray selection of bright AGN brings out mainly so-called Narrow-Line Seyfert 1 galaxies. Given the selection bias in favor of low intrinsic column density objects, type-1 Seyferts were strongly expected from the unified model for Seyfert galaxies in which type-2 Seyferts are seen through large absorbing column depths associated with molecular tori surrounding the central accretion black hole and therefore do not show up as strong soft

**Table 3.** Result of the principal component analysis (PCA) for 72 AGN of the soft X-ray selected ROSAT AGN sample

Property	E-vector 1	E-vector 2	E-vector 3
Eigenvalue	2.772	1.407	0.933
Proportion	0.396	0.201	0.133
Cumulative	0.396	0.597	0.730
$FWHM(H\beta_b)$	-0.145	+0.710	-0.187
$FWHM([OIII])$	+0.389	+0.073	-0.638
$[OIII]/H\beta_b$	-0.439	+0.048	-0.145
EW FeII	+0.312	-0.435	-0.452
$\alpha_x$	+0.375	-0.200	+0.381
$\alpha_{opt}$	-0.452	-0.243	-0.425
$\log \nu L_V$	+0.438	+0.447	-0.083

X-ray sources. Among the newly found ROSAT AGN, there is a peculiar trend with luminosity. The most luminous sources in the sample have the bluest optical continua, the steepest X-ray spectra, the broadest  $[OIII]$  but narrower  $H\beta_b$  line widths, the weakest  $[OIII]/H\beta_b$  flux ratios, and the strongest optical FeII blends. In Paper I we argued that these sources also seem to have the most pronounced Big Blue Bump spectra extending from optical wavelengths to soft X-rays peaking somewhere in the EUV<sup>3</sup>. We recall that some of the AGN in the sample also showed extreme X-ray variability and spectral changes (see also 4.3). The drawback with optical emission line studies is that they are sensitive to a very large number of physical parameters such as the kinematics, the density and temperature, and the composition of the emitting clouds, the ionizing continuum from the active nucleus and the properties of the ambient medium. Certainly, a new class of AGN could differ in all aspects from other well-known Seyfert galaxies, but in a more economic scheme one would like to see just one fundamental quantity to be responsible for the observed peculiarities. Among such quantities, those related to the accreting black hole paradigm (black hole mass, mass accretion rate, inclination angle, density of ambient medium, power of nuclear wind) seem to be the most promising in holding the clue to the explanation of the trends seen among the bright soft X-ray selected AGN.

##### 4.1. $FWHM(H\beta_b) - \alpha_x$ correlation

One of the most prominent relations found in X-ray-selected AGN samples is the trend for objects with steeper X-ray spectra to show narrower BLR lines. This does not necessarily hold the other way around: objects with narrow BLR lines may show both steep as well as flat X-ray spectra, while objects with broad emission lines always have flat X-ray spectra. This upper right part of Fig. 2 is, therefore, sometimes referred to as the 'zone of avoidance'. There are several possible explanations for this

<sup>3</sup> This trend does not seem to continue far into the quasar luminosity range. Quasar spectra bend sharply in the UV to meet the X-ray power laws (Zheng et al. 1997). Such a spectral shape cannot be accepted for the AGN in this study, since the extrapolation of the steep X-ray slopes toward the UV would imply unphysical luminosities in the EUV.

white spot on the map: a large mass of the central black hole, low inclination, or obscuration effects.

A simple explanation of the special nature of NLSy1 galaxies is a lower mass of the black hole compared to the black hole mass of other Sy 1s. Keplerian rotation of the BLR clouds would then proceed at comparatively small velocities and  $H\beta_b$  would be narrow. Lower-mass black holes produce soft X-ray spectra for two reasons. First, due to the  $T \propto (\dot{M}/M)^{1/4}$  relation (e.g. Laor & Netzer 1989, Ross et al. 1992), such black holes would result in a hotter accretion disc, and second, in order to reach a high luminosity it would have to accrete closer to its Eddington limit, causing the X-ray spectrum to become steep (e.g. Ross et al. 1992).

Another explanation of the  $\alpha_x - \text{FWHM}(H\beta_b)$  relation can be that the size of the BLR is different in NLSy1s compared to ‘normal’ Seyfert 1s. Wandel (1997) and Wandel & Boller (1998) suggested that the size of the BLR and therefore the distance of the BLR clouds to the center is directly related to the shape of the X-ray spectrum. In their model, the occurrence of steep X-ray spectra increases with luminosity. Low-luminosity NLSy1s would be those with flat X-ray spectra. This is in agreement with our finding of no correlation between  $\alpha_x$  and  $H\beta_b$  for the low-luminosity AGN.

Orientation effects can also play a role to explain the  $\alpha_x - \text{FWHM}(H\beta_b)$  relation. Wills & Browne (1986) showed that the BLR seems to be flattened. The X-rays are thought to be emitted from the inner part of an accretion disk. If this disk is thicker in the inner part, looking at low inclination angles would lead to narrow emission lines from the BLR and higher X-ray fluxes at soft X-ray energies. At higher inclination angles, we would see broader lines and flatter X-ray spectra.

Related to orientation effects is also the possibility that the high-velocity clouds in NLSy1 may be obscured. Our measurement of the Balmer decrements does not support this view nor is there significant polarization indicative of scattering in an obscuring medium (Grupe et al. 1998b).

In summary, the observed  $\alpha_x - \text{FWHM}(H\beta_b)$  relation is consistent with several simple schemes. The fact, however, that the narrow  $H\beta$  lines typically go along with strong FeII emission line strength, low  $[\text{OIII}]/H\beta_b$ , and steep X-ray spectra calls for a more involved explanation.

#### 4.2. Other correlations

The Principal Component Analysis shows that the common trend among the correlations between the various emission line and continuum properties is indeed dominated by the variation of one fundamental quantity, as can be seen from the dominance of Eigenvector 1 (EV1). This corroborates results from from differently selected NLSy1s using the same statistical analysis technique (Boroson & Green 1992, Laor et al. 1997). This parameter is not the inclination angle (Lawrence et al. 1997) which was already rejected based on the missing polarization, lack of internal soft X-ray absorption, and the uncorrelated Balmer decrements, since the  $[\text{OIII}]$  flux (believed to be a robust indicator of the isotropic flux) should then be independent of EV1

contrary to the result of the analysis. In principle, the accretion rate in units of the Eddington accretion rate works well to drive the correlations by increasing the Big Blue Bump strength and by decreasing the Balmer line width, but some additional element connected with the higher accretion rate is missing in order to explain the other contributions to EV1. This missing element could be the density of the ambient medium, the power of a nuclear wind, or the duration of the near-Eddington episodes of the accretion mode. Near-Eddington accretion could require that the central gas density is higher. The higher electron density could drive the correlation between luminosity and  $\text{FWHM}(\text{OIII})$  (Fig. 3) provided that the ionizing luminosity averaged over the light-crossing time of the NLR ( $\sim 100$  years) is much lower than the observed luminosity (to account for the weakness of the NLR). This means that one would have to require that the high-states are of a transient nature (as observed in a few individual cases). The other properties that go with Eigenvector 1 then follow naturally from the enhanced accretion rate. The scenario also accounts for the minor effect on  $\text{FWHM}(H\beta_b)$ , since the increase in electron density is compensated by the increase in luminosity in the vicinity of the accretion disk (i.e. if  $t_{\text{dur}} \geq t_{\text{BLR}} \sim \text{months}$ ). The higher density could also be a secondary effect associated with the higher accretion rate in NLSy1s. Lawrence et al. (1997) suggested that EV1 could reflect the effect of the density of an out-flowing wind. They argue that ‘the low-excitation of at least the BLR results from gas that is mechanically heated rather than radiatively heated’. There are several observations that seem to support this picture. First of all, outflows in AGN are observed in an increasing number of sources. Speaking for this is the finding of UV absorption lines in WPVS007 and RX J0134.2–4258 (Goodrich et al. 1999, in prep), the AGN with the steepest X-ray spectra during the RASS. Recently it was also reported that the Eigenvector 1 found in the PG sample of Laor et al. (1997) is rather strongly related to a unique density indicator,  $(\text{SiIII})/(\text{CIII})$  (B.J. Wills, private communication). Similarly, Smith (1993) argued for a nuclear wind that pushes the lighter clouds outwards. These can form the NLR, while heavier clouds would fall inwards. In the profiles of the  $[\text{OIII}]$  line we see a blue-shifted base in the weaker lines which may be related to these suggestions. However, blending of  $[\text{OIII}]\lambda 5007$  underlying FeII is important and contamination by some not so well understood component of the Fe complex can not be ruled out.

Alternatively, we may speculate that Eigenvector 1 represents the age of an AGN. It is likely that the appearance as an AGN is a short-lived phenomenon that can occur in every galaxy, rather than a long-lived phenomenon in only a few systems (Bechtold et al. 1994). If we assume that Eigenvector 1 is the age this would result in a higher accretion rate and probably stronger out-flowing wind at the beginning of the AGN’s life, implying that our soft X-ray selected AGN are relatively young. The age would nicely connect the properties that can be explained with the accretion rate with those that seem to be connected with outflows.



### 4.3. Transient soft X-ray AGN

Soft X-ray AGN and in particular NLSy1s often appear to be rapidly variable in X-rays (see e.g. Boller et al. 1993, 1997, and Leighly 1999). It should be noted that three of the sources of our bright soft X-ray AGN sample appear to be transient in X-rays. While IC 3599 has shown an outburst in X-rays with a response in its optical lines (Brandt et al. 1995. Grupe et al. 1995a), WPVS007, the AGN with the softest X-ray spectrum seen during the RASS was practically off in a pointed observation three years later (Grupe et al. 1995b). The third source, RX J0134.2–4258, is somewhat different. While its count rate in the ROSAT band remained nearly constant its X-ray spectrum changed completely between its RASS and a pointed observation two years later (Mannheim et al. 1996; Grupe et al. 1999). We found that it is the hard component that is mostly responsible for the peculiar spectral behavior of this AGN. In hard X-ray surveys this source would appear to be transient as well. All the other sources of our sample do not show significant variations either in X-rays or in the optical spectral range.

## 5. Summary and conclusions

We have studied the emission line properties of a sample of 76 bright soft X-ray-selected AGN and found that

- they are Seyfert 1s preferably with relatively narrow BLR emission lines,
- there is a general trend that the steep X-ray spectra also go along with blue optical continua, weak forbidden emission lines, strong optical FeII blends, and high luminosities,
- this trend seems to be driven by one or very few physical properties (Eigenvector 1 in a principal component analysis accounts for 40% of the intrinsic variance of the data),
- the accretion rate in units of the Eddington accretion rate most certainly is one basic driver behind Eigenvector 1,
- short-lived states (months to years) of a higher than usual accretion rate and higher electron densities of the emission line clouds possibly associated with nuclear winds could play a role for the observed trends.

This paper can be retrieved via WWW from our pre-print server: <http://eden.uni-sw.gwdg.de/preprints/preprints.html> and <http://www.xray.mpe.mpg.de/dgrupe/research/refereed.html>

*Acknowledgements.* We thank Dr. Klaus Reinsch for taking part of the optical spectra, Dr. Beverley Wills for providing the Boroson & Green FeII template and for numerous helpful comments, and Drs. Karen Leighly, Stefanie Komossa, and Thomas Boller for useful suggestions and discussions. Special thanks go also to David Doss, Jerry Martin, Marian Frueh, and Doug Otupal at McDonald Observatory for their instrumental and observing help. This research has made use of the NASA/IPAC Extragalactic Database (NED) which is operated by the Jet Propulsion Laboratory, Caltech, under contract with the National Aeronautics and Space Administration. Also we used the IRAS data request of the Infrared Processing and Analysis Center (IPAC) Caltech. This research was first supported by the DARA under grant 50 OR 92 10 and later sponsored by the Bundesanstalt für Arbeit. The

ROSAT project is supported by the Bundesministerium für Bildung und Forschung (BMBF) and the Max-Planck-Gesellschaft.

## Appendix A: optical spectra

The instrument mounted at the telescope was the ESO Faint Object Spectrograph and Camera (EFOSC2) fitted out with the following gratings:

- #1: 3400–9200 Å; 8.4 Å/pix  $\approx$  22 Å FWHM resolution (1.5" slit)
- #4: 4650–6800 Å; 2.2 Å/pix  $\approx$  7 Å FWHM resolution
- #8: 4640–5950 Å; 1.3 Å/pix  $\approx$  5 Å FWHM resolution
- #9: 5875–7020 Å; 1.1 Å/pix  $\approx$  5 Å FWHM resolution
- #10: 6600–7820 Å; 1.2 Å/pix  $\approx$  5 Å FWHM resolution

The EFOSC CCD camera was equipped with a THX 1024×1024 CCD with 19  $\mu$ m squared pixels.

The observations of all northern AGN were performed with the 2.1m Otto Struve telescope at the McDonald Observatory/West-Texas (MCD2.1 in Table A1), which is run by the University of Texas at Austin. For these observations, the Cassegrain Spectrograph ES2 was mounted at the telescope. During the March 1994 observing run, grating #22 (114 Å/mm  $\approx$  4 Å FWHM resolution) was used to examine the wavelength range between 4650 to 6050 Å. The camera was equipped with the CC1 CCD (1024×1024; 12×12  $\mu$ m<sup>2</sup> pixel size).

## Appendix B: FeII subtracted spectra

In this part of the appendix we present the FeII subtracted spectra. The FeII contaminated spectrum and the FeII template are plotted with an offset. The upper most spectrum is the original FeII containing one, the middle one shows the FeII subtracted spectrum and the lower spectrum is the FeII template used for the object. A description of the FeII subtraction is given in Sect. 2.2.

## References

- Bechtold J., Elvis M., Fiore, F., et al., 1994, AJ 108, 759  
 Beuermann K., Thomas H.-C., Reinsch K., et al., 1999, A&A accepted  
 Boller Th., Trümper J., Molendi S., et al., 1993, A&A 279, 53  
 Boller Th., Brandt W.N., Fink H.H., 1996, A&A 305, 53  
 Boller Th., Brandt W.N., Fabian A.C., Fink H.H., 1997, MNRAS 289, 393  
 Boroson T.A., Green R.F., 1992, ApJS 80, 109  
 Brandt W.N., Boller, Th., 1998, Astro. Nachr. 319, 7  
 Brandt W.N., Pounds K.A., Fink H.H., 1995, MNRAS 273, L47  
 Brotherton M.S., 1996, ApJS 102, 1  
 Córdova F.A., Kartje J.F., Thompson R.J., et al., 1992, ApJS 81, 661  
 Ferland G.J., Osterbrock D.E., 1986, ApJ 300, 658  
 Francis P.J., Hewett P.C., Foltz C.B., Chaffey F.H., 1992, ApJ 398, 476  
 Goodrich R.W., 1989a, ApJ 340, 190  
 Goodrich R.W., 1989b, ApJ 342, 224  
 Grupe D., 1996, Ph.D. Thesis, Göttingen University, (available via <http://www.xray.mpe.mpg.de/dgrupe/research/thesis.html>)  
 Grupe D., Beuermann K., Mannheim K., et al., 1995a, A&A 299, L5  
 Grupe D., Beuermann K., Mannheim K., et al., 1995b, A&A 300, L21

**Table A1.** List of the optical observations of the objects of the soft X-ray AGN sample. ESO2.2 = ESO/MPI 2.2m telescope, La Silla; MCD2.1 = 2.1m telescope McDonald Observatory, Texas; EFOSC = ESO Faint Object Spectrograph and Camera, ES2 = McDonald Cassegrain Spectrograph. The numbers given behind the instrument indicate the used grisms or gratings. The exposure time  $T_{\text{exp}}$  is given in minutes.

No.	Object	$\alpha_{2000}$	$\delta_{2000}$	obs. date	Tel.	Instrument	$T_{\text{exp}}$
1	RX J0022-34	00 22 33	-34 07 22	93/10/11	ESO2.2	EFOSC 1,8,10	10,45,45
2	ESO242-G8	00 25 01	-45 29 55	93/09/14	ESO2.2	EFOSC, 1,8,10	5,30,30
3	WPVS007	00 39 16	-51 17 03	93/01/01	ESO2.2	EFOSC, 1,8,10	5,20,20
4	RX J0057-22	00 57 20	-22 22 56	92/10/17	ESO2.2	EFOSC, 1,8,10	5,30,30
5	QSO0056-36	00 58 37	-36 06 06	93/10/12	ESO2.2	EFOSC 1,8,10	10,25,20
6	RX J0100-51	01 00 27	-51 13 55	93/10/12	ESO2.2	EFOSC, 1,8,10	10,40,35
7	MS0117-28	01 19 36	-28 21 31	93/10/14	ESO2.2	EFOSC, 1,9	5,30
8	IRAS01267-2157	01 29 11	-21 41 57	93/12/18	ESO2.2	EFOSC 1,8,10	5,30,20
9	RX J0134-42	01 34 17	-42 58 27	93/12/18	ESO2.2	EFOSC, 1,8,9	5,30,30
10	RX J0136-31	01 36 54	-35 09 53	93/12/18	ESO2.2	EFOSC, 1,4	10,30
11	RX J0148-27	01 48 22	-27 58 26	92/08/26	ESO2.2	EFOSC, 8,10	15,15
12	RX J0152-23	01 52 27	-23 19 54	93/09/12	ESO2.2	EFOSC, 1,8,10	5,30,30
13	RX J0204-51	02 04 03	-51 04 57	93/10/14	ESO2.2	EFOSC, 1,4	10,30
14	RX J0228-40	02 28 15	-40 57 16	92/10/18	ESO2.2	EFOSC, 1,10	5,30
15	RX J0319-26	03 19 49	-26 27 13	92/10/18	ESO2.2	EFOSC, 1,8,10	5,30,30
16	RX J0323-49	03 23 15	-49 31 15	93/08/21	ESO2.2	EFOSC, 1,8,10	30,30,30
17	ESO301-G13	03 25 02	-41 54 18	93/09/13	ESO2.2	EFOSC 1,8,10	5,45,45
18	VCV0331-37	03 33 40	-37 06 55	93/09/14	ESO2.2	EFOSC 1,8,10	5,30,30
19	RX J0349-47	03 49 08	-47 11 05	93/10/11	ESO2.2	EFOSC 1,9	10,40
20	Fairall 1116	03 51 42	-40 28 00	93/10/12	ESO2.2	EFOSC, 1,8,10	5,30,20
21	RX J0412-47	04 12 41	-41 12 46	93/10/19	ESO2.2	EFOSC, 1,8,10	5,30,30
22	RX J0426-57	04 26 01	-57 12 02	93/09/14	ESO2.2	EFOSC, 1,8,10	5,20,15
23	Fairall 303	04 30 40	-53 36 56	93/10/10	ESO2.2	EFOSC 1,8,10	5,30,20
24	RX J0435-46	04 35 14	-46 15 33	93/12/18	ESO2.2	EFOSC, 1,4	5,30
25	RX J0435-36	04 35 54	-36 36 41	93/10/14	ESO2.2	EFOSC 1,4	5,30
26	RX J0437-47	04 37 28	-47 11 29	92/08/26	ESO2.2	EFOSC 8,10	15,15
27	RX J0438-61	04 38 29	-61 47 59	93/10/11	ESO2.2	EFOSC, 1,8,10	5,15,20
28	RX J0439-45	04 39 45	-45 40 42	93/10/12	ESO2.2	EFOSC, 1,8,9	10,40,35
29	RX J0454-48	04 54 43	-48 13 20	93/10/14	ESO2.2	EFOSC, 1,4	10,30
30	RX J1005+43	10 05 42	+43 32 41	94/03/07	MCD2.1	ES2, 22	45
31	CBS 126	10 13 03	+35 51 24	94/03/06	MCD2.1	ES2, 22	45
32	RX J1014+46	10 14 02	+46 19 54	94/03/08	MCD2.1	ES2, 22	45
33	RX J1017+29	10 17 18	+29 14 34	94/03/07	MCD2.1	ES2, 22	35
34	Mkn 141	10 19 13	+63 58 03	94/03/06	MCD2.1	ES2, 22	30
35	Mkn 142	10 25 31	+51 40 35	94/03/07	MCD2.1	ES2, 22	40
36	RX J1050+55	10 50 55	+55 27 23	94/03/08	MCD2.1	ES2, 22	45
37	EXO1055+60	10 58 30	+60 16 01	94/03/08	MCD2.1	ES2, 22	45
38	RX J1117+65	11 17 10	+65 22 07	94/03/08	MCD2.1	ES2, 22	45
39	Ton 1388	11 19 09	+21 19 18	94/03/06	MCD2.1	ES2, 22	45
40	Mkn 734	11 21 47	+11 44 19	94/03/07	MCD2.1	ES2, 22	30
41	Z 1136+34	11 39 14	+33 55 52	94/03/07	MCD2.1	ES2, 22	35
42	CSO 109	11 45 10	+30 47 17	94/03/08	MCD2.1	ES2, 22	45
43	RX J1231+70	12 31 37	+70 44 14	94/03/08	MCD2.1	ES2, 22	30
44	IC 3599	12 37 41	+26 42 28	94/03/06	MCD2.1	ES2, 22	45
45	IRASF1239+33	12 42 11	+33 17 03	94/03/07	MCD2.1	ES2, 22	40
46	RX J1312+26	13 12 59	+26 28 27	94/03/07	MCD2.1	ES2, 22	45
47	RX J1314+34	13 14 23	+34 29 40	94/03/06	MCD2.1	ES2, 22	45
48	RX J1355+56	13 55 17	+56 12 45	94/03/08	MCD2.1	ES2, 22	45
49	RX J1413+70	14 13 37	+70 29 51	94/03/06	MCD2.1	ES2, 22	35
50	Mkn 684	14 31 05	+28 17 15	94/03/07	MCD2.1	ES2, 22	30
51	Mkn 478	14 42 08	+35 26 23	94/03/06	MCD2.1	ES2, 22	45
52	RX J1618+36	16 18 09	+36 19 58	94/03/08	MCD2.1	ES2, 22	45
53	RX J1646+39	16 46 26	+39 29 33	94/03/08	MCD2.1	ES2, 22	30
54	RX J2144-39	21 44 06	-39 49 01	92/08/21	ESO2.2	EFOSC, 1,8,10	30,30,30
55	RX J2154-44	21 54 51	-44 14 06	92/10/18	ESO2.2	EFOSC, 1,9	5,30

**Table A1.** (continued)

No.	Object	$\alpha_{2000}$	$\delta_{2000}$	obs. date	Tel.	Instrument	$T_{\text{exp}}$
56	RX J2213–17	22 13 00	–17 10 18	93/08/20	ESO2.2	EFOSC, 1,8,10	10,30,15
57	RX J2216–44	22 16 53	–44 51 57	92/10/17	ESO2.2	EFOSC, 1,8,10	5,30,30
58	RX J2217–59	22 17 57	–59 41 30	93/09/14	ESO2.2	EFOSC, 1,8,10	10,45,45
59	RX J2221–27	22 21 49	–27 13 10	93/10/14	ESO2.2	EFOSC, 1,4	10,30
60	RX J2232–41	22 32 43	–41 34 37	93/10/10	ESO2.2	EFOSC, 1,8,10	10,40,40
61	RX J2241–44	22 41 56	–44 04 55	93/10/12	ESO2.2	EFOSC, 1,10	10,40
62	RX J2242–38	22 42 38	–38 45 17	93/10/11	ESO2.2	EFOSC, 1,8,9	5,45,45
63	RX J2245–46	22 45 20	–46 52 12	92/10/18	ESO2.2	EFOSC, 1,8,9	5,30,30
64	RX J2248–51	22 48 41	–51 09 53	92/10/19	ESO2.2	EFOSC, 1,8,10	5,30,30
65	MS2254–37	22 57 39	–36 06 07	93/09/12	ESO2.2	EFOSC, 1,8,10	5,30,30
66	RX J2258–26	22 58 45	–26 09 14	92/08/26	ESO2.2	EFOSC, 1,8,10	15,20,20
67	RX J2301–55	23 01 52	–55 08 31	92/10/19	ESO2.2	EFOSC, 1,8,10	,40,25
68	RX J2303–55	23 03 58	–55 17 18	92/08/24	ESO2.2	EFOSC, 1,8,10	20,30,30
69	RX J2304–35	23 04 37	–35 01 13	92/08/25	ESO2.2	EFOSC, 1,8,10	15,30,30
70	RX J2304–51	23 04 39	–51 27 59	93/09/10	ESO2.2	EFOSC, 1,8,10	5,45,30
71	RX J2317–44	23 17 50	–44 22 27	93/10/12	ESO2.2	EFOSC, 1,8,10	10,40,30
72	RX J2325–32	23 25 12	–32 36 36	93/10/14	ESO2.2	EFOSC, 1,4	5,30
73	RX J2340–53	23 40 23	–53 28 57	93/10/14	ESO2.2	EFOSC, 1,4	5,30
74	MS2340–15	23 43 29	–14 55 31	93/09/14	ESO2.2	EFOSC, 1,8,10	5,30,30
75	RX J2349–33	23 49 07	–33 11 45	93/10/13	ESO2.2	EFOSC, 1,8	10,40
76	RX J2349–31	23 49 24	–31 26 03	93/08/21	ESO2.2	EFOSC, 1,8,10	30,30,30

Grupe D., Beuermann K., Mannheim K., Thomas H.-C., Fink H.H., 1998a, A&A 330, 25 (Paper I)

Grupe D., Wills B.J., Wills D., Beuermann K., 1998b, A&A 333, 827

Grupe D., Leighly K.M., Thomas H.-C., Laurent-Muehleisen S.A., 1999, A&A submitted

Komossa S., Bade N., 1999, A&A in press

Laor A., Netzer H., 1989, MNRAS 238, 897

Laor A., Fiore F., Elvis M., Wilkes B., McDowell J.C., 1994, ApJ 435, 611

Laor A., Fiore F., Elvis M., Wilkes B., McDowell J.C., 1997, ApJ 477, 93

Lawrence A., Elvis M., Wilkes B.J., McHardy I., Brandt N., 1997, MNRAS 285, 879

Leighly K.M., 1999, ApJ submitted

Mannheim K., Grupe D., Beuermann K., Thomas H.-C., Fink H.H., 1996, In: MPE Report 263, Röntgenstrahlung from the Universe. p. 471

Osterbrock D.E., 1989, Astrophysics of Gaseous Nebulae and Active Galactic Nuclei. University Science Books, Mill Valley, California

Osterbrock D.E., Pogge R.W., 1985, ApJ 297, 166

Phillips M.M., 1978a, ApJ 226, 736

Phillips M.M., 1978b, ApJS 38, 187

Pfeffermann E., Briel U.G., Hippmann H., et al., 1986, SPIE 733, 519

Puchnarewicz E.M., Mason K.O., Córdova F.A., et al., 1992, MNRAS 256, 589

Ross R.R., Fabian A.C., Mineshige S., 1992, MNRAS 258, 189

Smith S.J., 1993, ApJ 411, 570

Stephens S.A., 1989, AJ 97, 10

Thomas H.-C., Beuermann K., Reinsch K., et al., 1998, A&A in press

Trümper J., 1983, Adv. Space Res. 4, 241

Voges W., 1993, Adv. Space. Res. 13, 391

Voges W., Aschenbach B., Boller Th., et al., 1999, A&AS in press

Wandel A., 1997, ApJ 490, L131

Wandel A., Boller Th., 1998, A&A 331, 884

Whitney C.A., 1983a, A&AS 51, 443

Whitney C.A., 1983b, A&AS 51, 463

Wills B.J., Browne I.W.A., 1986, ApJ 302, 56

Zheng W., Kriss G.A., Telfer R.C., Grimes J.P., Davidson A.F., 1997, ApJ 475, 469